A major purpose of the Technical Information Center is to provide the broadest dissemination possible of information contained in DOE's Research and Development Reports to business, industry, the academic community, and federal, state and local governments.

Although a small portion of this report is not reproducible, it is being made available to expedite the availability of information on the research discussed herein.

LA-UR -84-1586
CONF-8404146--4

NOTICE

PORTIONS OF THIS REPORT ARE ILLEGIBLE. It has been reproduced from the best available copy to permit the broadest possible availability.

Los Alamos National Laboratory is operated by the University of California for the United States Department of Energy under contract W-7405-ENG-36.

LA-UR--84-1586

DE84 012439

TITLE: NUMERICAL FLUID DYNAMICS CALCULATIONS OF NONEQUILIBRIUM STEAM-WATER FLOWS WITH ENTRAINED DROPLETS

AUTHOR(S): Kenneth A. Williams

SUBMITTED TO: The International Workshop on Fundamental Aspects of Post-Dryout Heat Transfer, Salt Lake City, UT, April 1-4, 1984.

DISCLAIMER

Los Alamos Los Alamos National Laboratory
Los Alamos, New Mexico 87545

FORM NO 836 R4
ST NO 2629 6/81

NUMERICAL FLUID DYNAMICS CALCULATIONS OF NONEQUILIBRIUM STEAM-WATER FLOWS WITH ENTRAINED DROPLETS*

by

K. A. Williams
Deputy Group Leader
Thermal Hydraulics Group

Energy Division
Los Alamos National Laboratory

ABSTRACT

An improved thermal-hydraulic modeling capability for the engineering analysis of nonequilibrium steam-water flows with entrained droplets has been developed. An efficient numerical fluid dynamics method was formulated that solves the conservation equations of a four-field model consisting of a vapor field, a continuous liquid field, and two dispersed droplet fields, (e.g., an annular flow situation with droplets being entrained from the liquid film). The numerical method advances a two-field (vapor/liquid) formulation for two-phase flows such that the additional field equations are efficiently solved without increasing the size of the matrix problem. Conservation equations for mass and momentum are included for two additional liquid fields to represent dispersed droplets of two different sizes. The thermal characteristics of the liquid phases are represented with a single energy equation; however, the interfacial heat transfer between the vapor and the three liquid fields is evaluated separately for each field based on its own surface area and heat transfer coefficient. Also, interfacial surface area transport equations were solved for each droplet field resulting in an accurate calculation of the interfacial surface area as drops move through the Eulerian computational mesh.

Assessment of the present work concentrated on predicting the thermal-hydraulics of steam-water-droplet flows in a post-critical-heat-flux experimental test section with superheated walls. This work was shown to be in good agreement with experimental measurements of significant thermal nonequilibrium between the vapor and dispersed droplets. The tests analyzed covered a range of mass fluxes and wall heating rates but were all at low pressures where nonequilibrium effects are most pronounced. The present work predicted the vapor superheating in all tests to within an error range of -12% to +7.4%.

*Work performed under the auspices of the United States Nuclear Regulatory Commission.

NUMERICAL FLUID DYNAMICS CALCULATIONS OF NONEQUILIBRIUM STEAM-WATER FLOWS WITH ENTRAINED DROPLETS*

by

K. A. Williams
Deputy Group Leader
Thermal Hydraulics Group

Energy Division
Los Alamos National Laboratory

INTRODUCTION

Over the past decade there has been remarkable progress in the development and application of advanced numerical fluid dynamics methods for nuclear reactor safety issues. These so-called "advanced computer codes" model the two-phase thermal-hydraulic phenomena in a mechanistic manner accounting for nonequilibrium effects between the liquid and vapor phases.

In the context of the present work the term "nonequilibrium" implies that the vapor phase and the liquid phase may not be in thermal equilibrium with each other or with the local saturation temperature, and furthermore that relative motion may exist between these phases. For example, a boiling two-phase mixture in a heated channel may exist with the vapor significantly superheated while moving relative to saturated liquid droplets. Recent experimental results have demonstrated that vapor superheats of over 311°C can exist even in highly dispersed droplet flows with low qualities [1].

---

*This work was performed under the auspices of the United States Nuclear Regulatory Commission.

The present work is concerned with the numerical fluid dynamics of such nonequilibrium steam-water flows with entrained droplets. Modeling a vapor field flowing with three liquid fields consisting of a continuous liquid film or pool and droplets of two different sizes is of primary concern. A method for extending a state-of-the-art numerical technique [2] to this objective is developed and assessed against experimental measurements of thermal nonequilibrium effects in a post-critical-heat-flux test facility [3,4,5].

PREVIOUS WORK

Previous work on modeling steam-water flows in which nonequilibrium effects are important can be grouped into two separate classes: numerical fluid dynamics codes and correlations.

Over the last decade there has been remarkable progress made in numerical modeling of two-phase flow. One of the early, and most significant, numerical techniques capable of describing the solution of fluid flow problems in which several fields interact with one another was the implicit, multifield (IMF) solution method of Harlow and Amsden [6]. Improvements to the IMF technique were made by Rivard and Torry [7]. An overview of multifluid flow calcuational methods has been conducted by Stewart [8]. He concluded that the semi-implicit method developed by Liles and Reed [2] is "the most coherent numerical technique for smooth two-phase flows". The overall philosophy behind the method is closely tied to the physics of flows. That is, during the iteration all the conservation equations for both phases are simultaneously updated, and both the thermal and caloric equations of state have already been included into the iteration. The present work extends this method from a two-field representation to a four-field model. However, this procedure results in the final matrix problem to be solved for the new time unknowns having the same size as in the two-field model. Therefore, the additional computational costs associated with the improved physics in the more detailed fluid dynamics are minimized.

A three-field model for general reactor safety analysis has been developed by Thurgood, et al. [9]. This approach is an extension of the method of Liles and Reed and considers a single droplet field.

Various workers have developed models that are specific to the case of dispersed droplet flows. These models have attempted to represent in a mechanistic way the thermal nonequilibrium of vapor-droplet flows. That is, they have accounted for the various paths of heat flow that can result in the superheating of the vapor phase. One of the earliest models was due to Laverly and Rohsenow who experimented with film boiling of liquid nitrogen [10]. Forslund and Rohsenow extended this work by including the effect of direct wall to droplet heat transfer [11]; a similar model was developed independently by Bennett, et al [12].

An early attempt to apply such nonequilibrium models to the prediction of heat transfer in nuclear fuel rods is due to Sun, Gonzalez-Santalo and Tien [13]. Their model included the combined effects of radiation and convective heat transfer to investigate the influence of droplet sizes on the calculated vapor superheating. Improvements to this approach were made by Wong and Hochrieter [14] for application to reflood heat transfer in pressurized water reactors.

To date the most complete model for dispersed droplet nonequilibrium flows is due to Moose and Ganic [15]. Their model is applicable to high vapor fraction dryout in vertical upflows. A single representative drop size was chosen to represent the effects of a detailed consideration to the droplet size distribution. The calculated results were compared to data for high pressure steam-water, nitrogen and Freon-12.

Several researchers have attempted to develop correlations capable of predicting the vapor superheat (or nonequilibrium quality) as a function of the initial and boundary conditions for a given system. The two most important efforts have been due to Groenveld and Delorme [16] and to Chen, Sundaram and Ozkaynak [5]. The empirical correlation of Grovenveld and Delorme is applicable only in the dry-wall region but has the correct asymptotic trends and may be extrapolated outside the range of data on which it is based. The correlation of Chen, et al. is more phenomenological in that it was developed on the basis of additive vapor and liquid heat transfer

mechanisms at the hot wall. A detailed model was considered for the heat transfer between the wall and liquid that represents liquid superheating, bubble nucleation and growth, and evaporation of the residual liquid film. These correlations predict heat flux, actual quality, and vapor temperature using known values of pressure, mass flow rate, equilibrium quality and wall temperature. However, Nijhawan, et al. show that such correlations cannot predict the wall heat flux to within an order of magnitude under some situations [3].

PRESENT WORK

The objective of the present work was to develop an improved thermal-hydraulic modeling capability for the engineering analysis of nonequilibrium steam-water flows with entrained droplets. An efficient numerical fluid dynamics method was formulated that solves the conservation equations for a four-field model consisting of a vapor field, a continuous liquid field, and two dispersed droplet fields, (e.g., an annular flow situation with droplets being entrained from the liquid film). Conservation equations for mass and momentum are included for two additional liquid fields to represent dispersed droplets of two different sizes. The philosophy is that the important thermal and hydraulic effects of a spectrum of drop sizes in a spray can be represented with two droplet groups. This is reasonable because most of the interfacial surface area is contained within the smaller diameter droplet group, and most of the mass is contained within the larger diameter droplet group. Within any computational mesh cell all three liquid fields exist at the same temperature and pressure. Thus, the thermal characteristics of the liquid phases can be represented with a single liquid energy equation; however, the interfacial heat transfer between the vapor and the three liquid fields is evaluated separately for each field based on its own surface area and heat transfer coefficient. The details of all aspects of the development and assessment of the present work are given in Ref. 17.

FIELD EQUATIONS AND MODELS

The field equations representing the conservation of mass, momentum, and energy in the present four-field model are the following:

Conservation of Mass

Vapor Field

$$\frac{\partial}{\partial t}(\alpha_v \rho_v) + \vec{\nabla}\cdot(\alpha_v \rho_v \vec{V}_v) = \Gamma \tag{1}$$

Continuous Liquid Field

$$\frac{\partial}{\partial t}(\alpha_\ell \rho_\ell) + \vec{\nabla}\cdot(\alpha_\ell \rho_\ell \vec{V}_\ell) = -(1-\eta_1-\eta_2)\Gamma - S \tag{2}$$

Droplet Field 1

$$\frac{\partial}{\partial t}(\alpha_{d1} \rho_\ell) + \vec{\nabla}\cdot(\alpha_{d1} \rho_\ell \vec{V}_{d1}) = -\eta_1\Gamma + S_1 \tag{3}$$

Droplet Field 2

$$\frac{\partial}{\partial t}(\alpha_{d2} \rho_\ell) + \vec{\nabla}\cdot(\alpha_{d2} \rho_\ell \vec{V}_{d2}) = -\eta_2\Gamma + S_2 \tag{4}$$

Conservation of Momentum

Vapor Field

$$\alpha_v \rho_v \frac{\partial \vec{V}_v}{\partial t} + \alpha_v \rho_v \vec{V}_v \cdot \vec{\nabla} \vec{V}_v = - \alpha_v \vec{\nabla} P - \vec{F}_{wv}$$

$$- \vec{F}_{i,v\ell} - \vec{F}_{i,vd1} - \vec{F}_{i,vd2} + [\Gamma \vec{V}] + \alpha_v \rho_v \vec{g} \qquad (5)$$

Continuous Liquid Field

$$\alpha_\ell \rho_\ell \frac{\partial \vec{V}_\ell}{\partial t} + \alpha_\ell \rho_\ell \vec{V}_\ell \cdot \vec{\nabla} \vec{V}_\ell = - \alpha_\ell \vec{\nabla} P - \vec{F}_{w\ell}$$

$$- \vec{F}_{i,\ell v} - [\Gamma_\ell \vec{V}] - [S \vec{V}] + \alpha_\ell \rho_\ell \vec{g} \qquad (6)$$

Droplet Liquid Field 1

$$\alpha_{d1} \rho_\ell \frac{\partial \vec{V}_{d1}}{\partial t} + \alpha_{d1} \rho_\ell \vec{V}_{d1} \cdot \vec{\nabla} \vec{V}_{d1} = - \alpha_{d1} \vec{\nabla} P - \vec{F}_{wd1}$$

$$- \vec{F}_{i,d1v} - [\Gamma_{d1} \vec{V}] + [S_1 \vec{V}] + \alpha_{d1} \rho_\ell \vec{g} \qquad (7)$$

Droplet Liquid Field 2

$$\alpha_{d2} \rho_\ell \frac{\partial \vec{V}_{d2}}{\partial t} + \alpha_{d2} \rho_\ell \vec{V}_{d2} \cdot \vec{\nabla} \vec{V}_{d2} = - \alpha_{d2} \vec{\nabla} P - \vec{F}_{wd2}$$

$$- \vec{F}_{i,d2v} - [\Gamma_{d2} \vec{V}] + [S_{d2} \vec{V}] + \alpha_{d2} \rho_\ell \vec{g} \qquad (8)$$

Conservation of Energy

Vapor Field

$$\frac{\partial}{\partial t}(\alpha_v \rho_v e_v) + \vec{\nabla}\cdot(\alpha_v \rho_v e_v \vec{V}_v) + P\vec{\nabla}\cdot(\alpha_v \vec{V}_v)$$

$$+ P\frac{\partial \alpha_v}{\partial t} = \dot{Q}_{wv} + \dot{Q}_{i,\ell v} + \dot{Q}_{i,d1v} + \dot{Q}_{i,d2v} + \Gamma h_{sat,v} \qquad (9)$$

Total Liquid Fields

$$\frac{\partial}{\partial t}[(1-\alpha_v)\rho_\ell e_\ell] + \vec{\nabla}\cdot(\alpha_\ell \rho_\ell e_\ell \vec{V}_\ell) + \vec{\nabla}\cdot(\alpha_{d1}\rho_\ell e_\ell \vec{V}_{d1})$$

$$+ \vec{\nabla}\cdot(\alpha_{d2}\rho_\ell e_\ell \vec{V}_{d2}) + P\vec{\nabla}\cdot[\alpha_\ell \vec{V}_\ell + \alpha_{d1}\vec{V}_{d1} + \rho_{d2}\vec{V}_{d2}] \qquad (10)$$

$$+ P\frac{\partial}{\partial t}(1-\alpha_v) = \dot{Q}_{w\ell} + \dot{Q}_{i,v\ell} + \dot{Q}_{i,vd1} + \dot{Q}_{i,vd2} - \Gamma h_{sat,\ell}$$

The above field equations describe only the conservation principles and do not describe the thermodynamic properties of the materials involved or the interfacial area transport. For the analysis to apply to a specific fluid it is necessary to specify the equations of state. It is assumed that there are general thermal and caloric equations of state of the form.

$$\rho_\ell = \rho_\ell(P, T_\ell) \qquad (11)$$

$$\rho_v = \rho_v(P, T_v) \qquad (12)$$

$$e_\ell = e_\ell(P, T_\ell) \tag{13}$$

$$e_v = e_v(P, T_v) \tag{14}$$

We also have the continuity consideration that the volume fractions of all phases must sum to unity,

$$\alpha_v + \alpha_\ell + \alpha_{d1} + \alpha_{d2} = 1 \tag{15}$$

$$(1-\alpha_v) = \text{total liquid volume fraction} \tag{16}$$

Accurately modeling the thermal and hydraulic characteristics of a size distribution of droplets was an important consideration in the present work. Therefore, the following interfacial surface area transport equations were solved for each droplet field.

$$\frac{\partial A_{i,d1}}{\partial t} + \vec{\nabla}\cdot(A_{i,d1}\vec{V}_{d1}) = \frac{6S_1}{\rho_\ell D_{d1}} - S_{T,d1} \tag{17}$$

(18)

$$\frac{\partial A_{i,d2}}{\partial t} + \vec{\nabla}\cdot(A_{i,d2}\vec{V}_{d2}) = \frac{6S_2}{\rho_\ell D_{d2}} - S_{T,d2}$$

This modeling approach results in an accurate calculation of the interfacial surface area as drops move through the Eulerian computational mesh. Models for the droplet volume mean diameter, upper-log-normal size distribution function, and entrainment rates developed by Ishii, et al. from air-water data were adapted to the present work [18,19]. The droplet size distribution was correlated in terms of the volume fraction oversize (Δ), defined as the volume fraction of the droplets having a diameter larger than D. Their correlation is,

$$\frac{d\Delta}{dy} = -\frac{0.884}{\sqrt{\pi}} e^{-0.781y^2} \tag{19}$$

with

$$y = \ln\left(\frac{2.13D}{D_{max}-D}\right) \tag{20}$$

The authors also developed a correlation for the volume mean diameter, D_{vm}, of the spray. At a diameter of D_{vm} there are an equal volume of droplets at diameters above and below D_{vm}. That is, D_{vm} is the droplet diameter corresponding to a volume fraction oversize of 0.5. Their correlation for the volume mean diameter in terms of the flow properties is,

$$D_{vm} = 0.0099\frac{\sigma}{\rho_g j_g^2} R_{e_g}^{2/3}\left(\frac{\rho_g}{\rho_\ell}\right)^{-1/3}\left(\frac{\mu_g}{\mu_\ell}\right)^{2/3} \tag{21}$$

where j_g is the gas volumetric flux (superficial velocity). With the above distribution it can be shown that,

$$\frac{D_{max}}{D_{vm}} = 3.13 \tag{22}$$

The interfacial drag between the vapor and the two droplet fields uses a C_D type drag relationship for a solid sphere with the Reynolds number based on the relative velocity between the vapor and each droplet. The interfacial drag between the vapor and continuous liquid for annular flow is given by Wallis' model [20].

The interfacial heat transfer coefficient is based on a Nusselt type correlation for steam-water flows due to Lee and Riley [21],

$$h_{iv} = \frac{k_v}{D_d} Nu_v = \frac{k_v}{D_d} [2 + 0.74 R_e^{0.5} P_r^{1/3}] \tag{23}$$

The Reynolds number is based on the relative velocity between the vapor and each droplet phase. The interfacial area per unit volume A_i comes directly from the interfacial area transport equations. For spherical droplets the following relationship must hold at any point,

$$A_i = \frac{6\alpha_d}{D_d} \tag{24}$$

In dispersed flows with heated walls the surface temperature is normally above the minimum stable film boiling temperature. However, some heat transfer directly from the wall to the droplets can occur due to collisions between the drops and the wall. The heat transfer in this regime is very difficult to model and has been the subject of numerous investigations. The model of Forslund and Rohsenow is used in the present work [22].

The field equations and constitutive models of the present work have now been presented. The finite-different representation of these equations and the numerical solution procedure is given in Ref. 17. The numerics are a direct extension of the method of Liles and Reed [2]. The algebraic

difference equations are first-order accurate in space and time and are differenced ver a staggered mesh. The resulting set of nonlinear equations are solved at each time step by a Newton iteration procedure. The important result here is that the number of linearized equations to be solved at each iteration are the same in the present four-field model as in a two-field formulation. At each computational mesh cell we obtained a set of four linearized equations involving the four unknowns P, α, T_ℓ and T_v of that mesh cell and the pressures of the six adjacent cells. These equations can be written in matrix from as,

$$\begin{bmatrix} x & x & x & x \\ x & x & x & x \\ x & x & x & x \\ x & x & x & x \end{bmatrix} \begin{bmatrix} P \\ \alpha \\ T_v \\ T_\ell \end{bmatrix} + \begin{bmatrix} x & x & x & x & x & x \\ x & x & x & x & x & x \\ x & x & x & x & x & x \\ x & x & x & x & x & x \end{bmatrix} \begin{bmatrix} P_1 \\ P_2 \\ P_3 \\ P_4 \\ P_5 \\ P_6 \end{bmatrix} = \begin{bmatrix} x \\ x \\ x \\ x \end{bmatrix} \qquad (25)$$

where the subscripts 1-6 designate the six surrounding cells in three dimensions. This system can be put into a reduced form by multiplying through by the triangular decomposition of the 4 x 4 matrix. Then the first equation will involve only the cell pressure and its' six neighbors pressure. The remaining three equations then relate the vapor fraction and temperatures to the pressures. The full set of pressure equations for all mesh cells constitute a seven-striped linear algebraic system of equations for the pressure in all mesh cells. An important property of this reduced pressure formulation is its diagonal dominance. All coupling between the mesh cells is expressed in the pressure equations matrix. It is emphasized that the above process can be carried out in one mesh cell at a time, storing only the 28 quantities per mesh cell that appear as X's in the 4 x 6 matrix and the right

hand side of Eq. 25. These coefficients must be retained so that T_ℓ, T_v, and α can be found from a back-substitution after the pressures have been determined from the pressure iteration.

The size of the matrix problem in a four-field model does not increase because of two reasons. First, although there are now four velocities, the momentum equations are used to eliminate new-time velocities in favor of new-time pressures. Secondly, all three liquid fields exist at the same temperature and pressure at any location and a single liquid energy equation can be used. The two additional mass conservation equations can be solved for the new-time droplet volume fractions at the end of an iteration since all unknowns in these equations have been determined. Thus, any additional computational costs associated with doubling the number of fields has been minimized. Computer timing studies show that the present four-field model requires only a 15-17 percent increase over the two-field model in computation time per mesh cell per time step.

ASSESSMENT

Assessment of the present work concentrated on predicting the thermal-hydraulics of steam-water-droplet flows in a post-critical-heat-flux experimental test section with superheated walls. Until recently such data have been particularly lacking for post-CHF flows at low pressures, low flow rates and low qualities where nonequilibirum effects are most pronounced. This is because measurement of the vapor temperature in dispersed droplet flows is extremely difficult. Any temperature sensor will tend to be quenched by the entrained liquid droplets which are near the local saturation temperature, therefore preventing detection of vapor superheating. Also, radiation heat transfer from the high temperature walls can introduce measurement errors.

Such experimental measurements have recently been taken at Lehigh University [3,4,5] in a forced convection boiling two-phase experimental test facility shown in Fig. 1. The test section for post-CHF flows consists of a vertical heated channel of Inconel-600 that is 150 cm in length with a 1.41 cm inside

diameter tube. The test section is located above a "hot patch" designed to ensure post-CHF flow conditions. Wall temperature measurements are provided at 7.5 cm intervals along the test section. Joule heating of the tube is supplied by direct current through the walls using a variable d-c power supply of 30 kW. The vapor superheat probe is located 130 cm above the inlet to the copper hot patch.

The tests performed at Lehigh University covered a range of operating conditions. Three specific tests were selected for assessment of the present work. These tests were chosen in concert with the experimenters to cover important operating ranges in which there was very reliable data [23]. The experimental tests are,

Test 138: High inlet quality, intermediate mass flux, intermediate power.

Test 134: High inlet quality, intermediate mass flux, high power.

Test 50: Low inlet quality, low mass flux, low power.

The operating conditions for these three experiments are summarized in Table I. In all tests there is the substantial nonequilibrium effect of vapor superheating by roughly 280°C-350°C. This nonequilibirum effect can be clearly seen by comparing the change in equilibrium quality to the change in actual quality. For test 138 the actual change in quality was only 0.064 while the equilibrium value was 0.233. The ratio of the two quality changes is termed by Chen as the "heat-partition ratio" (R_Q) and measures the fraction of total wall heat transfer that went into evaporating the liquid phase. Thus, R_Q varies from zero for complete lack of thermodynamic equilibrium to one for complete equilibrium. In test 138 the R_Q is 0.27, in test 134 the R_Q is 0.32 and in test 50 the R_Q is 0.62.

Test 134 is a parametric variation on wall heat flux relative to test 138. The total power was increased by 31 percent, however the vapor superheating only increased by 12 percent. The vapor velocity in the test section for these two tests is quite high producing significant entrainment. The thermal-hydraulic conditions of test 50 are much different from those of test 138 and 134. The low inlet quality, mass flux and power result in very low vapor velocities producing much less entrainment.

A one-dimensional input model of the Lehigh Univesity test facility used in the present numerical calculations is shown in Fig. 2. There are a total of twelve (12) computational mesh cells over a total length of 1.806 meters. The flow area is 1.5617×10^{-4} m^2 with a hydraulic diameter of 1.41 centimeters. Boundary conditions are supplied at the first and last mesh cells. Inlet mass flux and steam-water volume fractions are specified at cell number 1, the inlet plenum. Test section pressure is imposed at cell number 12, the outlet plenum. The heated test section extends from mesh cells 2 through 11 for a total length of 1.456 meters. Cell 2 represents the high thermal inertia hot patch. As shown in Fig. 2, the experimental location of zero (0.0 m) elevation corresponds to the beginning of cell 2 which in the model has an absolute elevation of 0.20 meters. Vapor probe data from the experiment are to be compared with computed parameters of mesh cell 10; this corresponds to a heated length above the inlet of 1.306 meters.

The calculated vapor temperature as a function of heated length in test 138 is shown in Fig. 3. On all such figures the test section inlet (bottom of hot patch) corresponds to 0.2 m, as discussed above. The vapor probes experimental result of 692 K is seen to be in satisfactory agreement with the calculated value of 657 K. Experimentally this corresponds to a nonequilibrium superheated state of 270°C. The calculated vapor superheat is 246°C, for a relative error of -12 percent.

In Fig. 4 experimental wall temperature mesurements (chained line) along the heated test section are compared to the calculated wall surface temperatures (solid line). The wall temperature drops about 75°C just downstream of the hot patch in both the data and the calculation due to a reduction in the linear heating rate in the test section. Along the test section the wall temperatures vary from about 650 K to 900 K. The calculated surface temperature is in close agreement with the data along the first half of the test section and then begins to exceed the data by roughly 75°C for the last half. However, it is very important to note that the axial variation of power being input to the steam-water flow in the calculations is in exact agreement with the experimental boundary conditions. That is, the total wall heat flux into the mixture is correct at all elevations. Any deviation in

wall temperature between the data and calculation arises from errors in the heat transfer coefficients and/or fluid conditions and not from the heat flux boundary conditions.

Calculated vapor volume fraction as a function of height is shown in Fig. 5 to increase rapdily downstream of the hot patch due to entrainent and boiling of the liquid film. Droplet field 1 (larger diameter drops) volume fraction and droplet field 2 (smaller diameter drops) are compared in Fig. 6. Both droplet fields have a rapidly increasing volume fraction near the hot patch due to entrainment of the liquid film; the droplet volume fractions then decrease as a result of evaporation and acceleration with the vapor flow.

The calculated vapor axial velocity profile is shown in Fig. 7 to increase from 11 m/s at the inlet to almost 20 m/s at the outlet. The vapor velocity is continuously increasing due to a relatively constant vapor generation rate from the evaporation of the liquid droplets and from heating of the vapor. Droplet velocities are compared in Fig. 8. At the test section exit the smaller drops are moving at 8 m/s while the larger drops have a velocity of 4.5 m/s; thus there is a substantial relative velocity between the vapor field and the droplets even at the end of the heated length.

The relative partitioning of heat flow from the wall into the four fields can be evaluated from the numerical calculation. The product of interfacial heat transfer coefficient and surface area (hA) for both droplet groups is shown in Fig. 9. From this figure it can be seen that the smaller droplet field contributes almost three times the interfacial heat flow as does the larger drop field. This effect was not unexpected and is part of the original motivation for having two droplet fields. The heat flow paths from the wall into the vapor and liquid fields at the elevation of the vapor probe are shown in Fig. 10. It can be seen that three-fourths of the wall heat flux is delivered directly to the vapor phase. One-fourth of the energy flow is absorbed directly by the droplets as a result of collisions with the wall. However, this wall-to-droplet energy transport mechanism is responsible for the majority of the evaporation of the liquid phase since the interfacial flow of energy from the superheated vapor is very small. Even with the vapor superheated by 246^{0}C the interfacial heat transfer amounts to only 8 percent of the wall heat flux.

This surprising finding of poor interfacial heat transfer between the superheated vapor and saturated droplets is responsible for the large nonequilibrium effects in these post-CHF experiments. To better understand why this occurs it is necessary to analyze the interfacial surface areaconcentrations of the droplets; these are shown in Fig. 11 to vary from 2 to 20 m^2/m^3. The "area concentration of the wall" is a useful comparison to obtain an appreciation of the magnitude of these numbers.

$$A_{i,wall} = \frac{\pi D \cdot L}{\frac{\pi D^2}{4} \cdot L} = 4/D \tag{26}$$

For this test section with a hydraulic diameter of 1.41 cm the wall surface area concentration is 284 m^2/m^3. Thus, the effective surface area of the droplets along the heated length is an order of magnitude less that the wall itself. This then is the reason for the low interphase heat transfer that produces the high nonequilibrium state.

Test number 134 was performed at conditions very near those of test 138 with the exception of the wall heating rate (total power). This test is therefore useful for assessing the ability of the present work to correctly predict the parametric effects of varying only the wall heat flux. The power input to the mixture was increased 31 percent from test 138 to test 134; however, the vapor superheat only increased by 12 percent. The calculated vapor temperature as a function of heated length is shown in Fig. 12. It can be seen that the calculated and measured vapor superheats at the probe elevation are in very good agreement. The experimental vapor temperature is superheated by 312°C while the present work predicts 321°C for a relative error of +2.9 percent.

The operating conditions of test number 50 make it completely different in a thermal-hydraulic standpoint from tests 134 and 138. The major difference is that the inlet quality is very low at 6.6 percent corresponding to an inlet vapor volume fraction of 96.98 percent. Thus the liquid volume fraction has been increased by a factor of 20 from the high quality tests 138 and 134. Additionally, the mass flux and power have both been reduced which produces an inlet vapor velocity almost an order of magnitude lower than the other two tests. Indeed the vapor velocity of only 2-3 m/s is not sufficient to entrain the liquid film in a continuous manner.

The calculated vapor temperature profile is shown in Fig. 13. The experimental vapor probe measured a vapor superheat of 350°C and the present work predicted a value of 375°C for a relative error of +7.4 percent. However, the high superheating in this test has arisen from a very low entrainment at its' operating conditions and not from a low interfacial heat transfer as in tests 134/138.

The numerical calculations of tests 134, 138, and 50 discussed above were all performed using exactly the same code. The assessment study would not be complete however without conducting a sensitivity study. The two items of primary concern are the nodalization of the input model and the choice of the "free parameter" D/D_{vm} serving as the dividing point between the two droplet fields.

Nodalization sensitivity is addressed by modifying the input model so that the length of cells downstream of the hot patch were doubled from the base value of 15 to 30 centimeters. The high quality, high power test 134 was recalculated using this coarse node input model. The calculated vapor superheat was then 322°C as compared to the base case value of 321°C. Thus the computed results for this test are essentially unchanged by the choice of a different nodalization for the input model.

The free parameter of the present four-field model is the selection of D/D_{vm} that is used to partition surface area and mass between the two droplet fields. In the above calculations this parameter was set at 1.0 for a base value. This produces a 50-50 distribution of mass into the two droplet fields, but 77 percent of the total surface area is associated with the smaller droplet field. A value of $D/D_{vm} = 0.4$ was chosen for the sensitivity study. This choice results in only 7 percent of the entrained mass going to the smaller droplets but this field still contains 22 percent of the total droplet interfacial surface area. Test number 134 was recalculated with only this change. A vapor superheat of 323°C was now obtained which is only slightly different from the 321°C obtained in the base case calculation. The model is therefore relatively insensitive to the free parameter choice of D/D_{vm} for this case in which all of the liquid film has been entrained. A greater sensitivity may occur under conditions of lower vapor velocity where only the small droplets are entrained.

SUMMARY

The present work has developed a computational fluid dynamics formulation that efficiently solves the conservation laws for a vapor field, a continuous liquid field, and two dispersed droplet fields. The thermal-hydraulic effects resulting from the exchange of mass, momentum and energy between the vapor and the dispersed droplet phases has been accurately modeled. This work is an advancement of the state-of-the-art for engineering analyses of nonequilibrium steam-water-droplet flows in heated channels. It is particularly applicable for boiling steam-water flows in which it is important to represent the effects of significant thermal nonequilibrium between the vapor and the liquid phases. This work was shown to be in good agreement with unique experimental measurements of significant thermal nonequilibrium between the vapor and dispersed droplets. The tests analyzed covered a range of mass fluxes and wall heating rates, and were all at low pressures where nonequilibrium effects are most pronounced.

REFERENCES

1. Nijhawan, S., Chen, J. C., Sundaram, R. K., and London, E. J., "Measurement of Vapor Superheat in Post-Critical-Heat-Flux Boiling," J. Heat Transfer, Vol. 102, August (1980).

2. Liles, D. R., and Reed, Wm. H., "A Semi-Implicit Method for Two-Phase Fluid Dynamics," J. Computational Physics 26, pp 390-407 (1978).

3. Nijhawan, S., Chen, J. C., and Sundaram, R. K., "Parametric Effects on Vapor Nonequilibrium in Post-Dryout Heat Transfer," ASME Paper 80-WA/HT-50, July (1980).

4. Evans, D., Webb, S., Chen, J. C., and Neti, S., "Experimental Data for Nonequilibrium Post-CHF Heat Transfer in a Vertical Tube," Tenth Water Reactor Safety Research Information Meeting, NUREG/CP-0041, Vol. 1, October (1982).

5. Chen, J. C., Sundaram, R. K., and Ozkaynak, F. T., "A Phenomenological Correlation for Post-CHF Heat Transfer," USNRC Report NUREG-0237, June (1977).

6. Amsden, A. A., and Harlow, F. H., "KACHINA: An Eulerian Computer Program for Multifield Fluid Flows," Los Alamos Scientific Laboratory Report LA-5680, Los Alamos, NM (1974).

7. Rivard, W. C., and Torrey, M. D., "K-FIX: A Computer Program for Transient Two-Dimensional, Two-Fluid Flow," Los Alamos Scientific Laboratory report LA-NUREG-6623, Los Alamos, NM (1976).

8. Stewart, H. Bruce, "Overview of Multifluid Flow Calculation Methods," presented at Army Research Office Workshop on Multiphase Flow, Aberdeen Proving Ground, Maryland, February 2-4, (1981).

9. Thurgood, M. J., Kelly, J. M., Basehore, K. L., and George, T. L., "COBRA-TF: A Three-Field Two-Fluid Model for Reactor Safety Analysis," 19th National Heat Transfer Conference, Orlando, Florida, July 27-30, (1980).

10. Laverty, W. F. and Rohsenow, W. M., "Film Boiling of Saturated Liquid Nitrogen Flowing in a Vertical Tube," J. Heat Trans. 89, pp 90-98 (1964).

11. Forslund, R. P. and Rohsenow, W. M., "Dispersed Flow Film Boiling," ASME Paper No. 68-HT-44 (1968).

12. Bennett, A. W., Hewitt, G. F., Kearsey, H. A., and Keeys, R. K. F., "Heat Transfer to Steam Water Mixtures Flowing in Uniformly Heated Tubes in which the Critical Heat Flux has been Exceeded," Report No. AERE-R 5373 Harwell Laboratory (1967).

13. Sun, K. H., Gonzalez-Santalo, J. M., and Tien, C. L., "Calculations of Combined Radiation and Convective Heat Transfer in Rod Bundles Under Emergency Cooling Condtions," J. Heat Transfer, pp. 414-420, August (1976).

14. Wong, S. and Hochreiter, L. E., "A Model for Dispersed Flow Heat Transfer During Reflood," 19th Nat. Heat Transfer Conference, Orlando, FL, July 27-30 (1980).

15. Moose, R. A. and Ganic, E. N., "On the Calculation of Wall Temperatures in the Post Dryout Heat Transfer Regime," Int. J. Multiphase Flow, 8, No., pp. 525-542 (1982).

16. Groeneveld, D. C. and Delorme, G. G. J., "Prediction of Thermal Nonequilibrium in the Post-dryout Regime," Nuclear Engineering and Design, 36, pp. 17-26 (1976).

17. Williams, K. A., "Numerical Fluid Dynamics of Nonequilibrium Water Flows with Droplets," Ph.D. Dissertation, The University of New Mexico, May 1983.

18. Ishii, M. and Mishima. K., "Correlation for Liquid Entrainment in Annular Two-Phase Flow of Low Viscous Fluid," Argonne National Laboratory Report ANL/RAS/LWR 81-2 March (1981). Also published as NUREG/CR-2885.

19. Kataoka, I., Ishii, M., and Mishima, K., "Generation and Size Distribution of Droplets in Gas-Liquid Annular Two-Phase Flow," Argonne National Laboratory Report ANL/NAS/LWR 81-3 September (1981).

20. Wallis, G. B., One-Dimensional Two-Phase Flow, McGraw-Hill, New York (1969).

21. Lee, K. and Riley, D. J., "The Evaporation of Water Droplets in Superheated Steam," J. Heat Transfer, November (1966).

22. Forslund, R. P. and Rohsenow, W. M., "Dispersed Flow Film Boiling." J. Heat Transfer, Vol. 90, No. 6 (1968).

23. Private Communications, Professor J. Chen, Lehigh University.

Symbols

A_i	interfacial surface area per unit volume.
C_D	drag coefficient
D	diameter
D_H	hydraulic diameters.
e	specific internal energy.
$\vec{F}$	momentum drag vector.
$\vec{g}$	gravity field.
h	heat transfer coefficient.
h	fluid enthalpy.
j	superficial velocity
k	thermal conductivity.
Nu	Nusselt number.
P	pressure.
Pr	Prandtl number
$\dot{Q}$	total rate of heat transfer.
Re	Reynolds number
S	total mass transfer rate due to liquid film entrainment.
S_1, S_2	mass transfer rate due entrainment of droplet field 1, field 2.
S_Γ	rate of interfacial surface area concentration (A_i) due to phase change.
t	time.
T	temperature.
x	quality
μ	fluid viscosity
Δ	droplet volume fraction oversize.
σ	surface tension.
ρ	density.
α_k	volume fraction of phase k.
Γ	total vapor generation rate from phase change
η_1, η_2	fraction of total phase change produced by droplet field 1, field 2.

Symbols and Operators

$\nabla\cdot$	divergence operator.
∇	gradient operator.

Subscript and Superscript

d,D,d1,d2	drop phase.
i	interface.
r	relative
s	saturation
v	vapor phase
w	wall
ℓ	liquid phase.

Table I. Summary of Lehigh University Post-CHF Tests

Test Number	P (bar)	G (kg/s-m²)	Q (kw/m²)	$x_{e,o}$ (%)	$x_{e,L}$ (%)	$x_{e,a}$ (%)	$\frac{\Delta x_a}{\Delta x_e}$	Tv,data (K)	Tv,calculation (K)
138	3.6	37.33	49.32	55.8	79.1	62.2	0.27	692	657
134	3.5	37.35	64.73	57.4	87.1	66.8	0.32	725	734
50	3.8	29.94	23.39	6.6	19.4	14.5	0.62	764	785

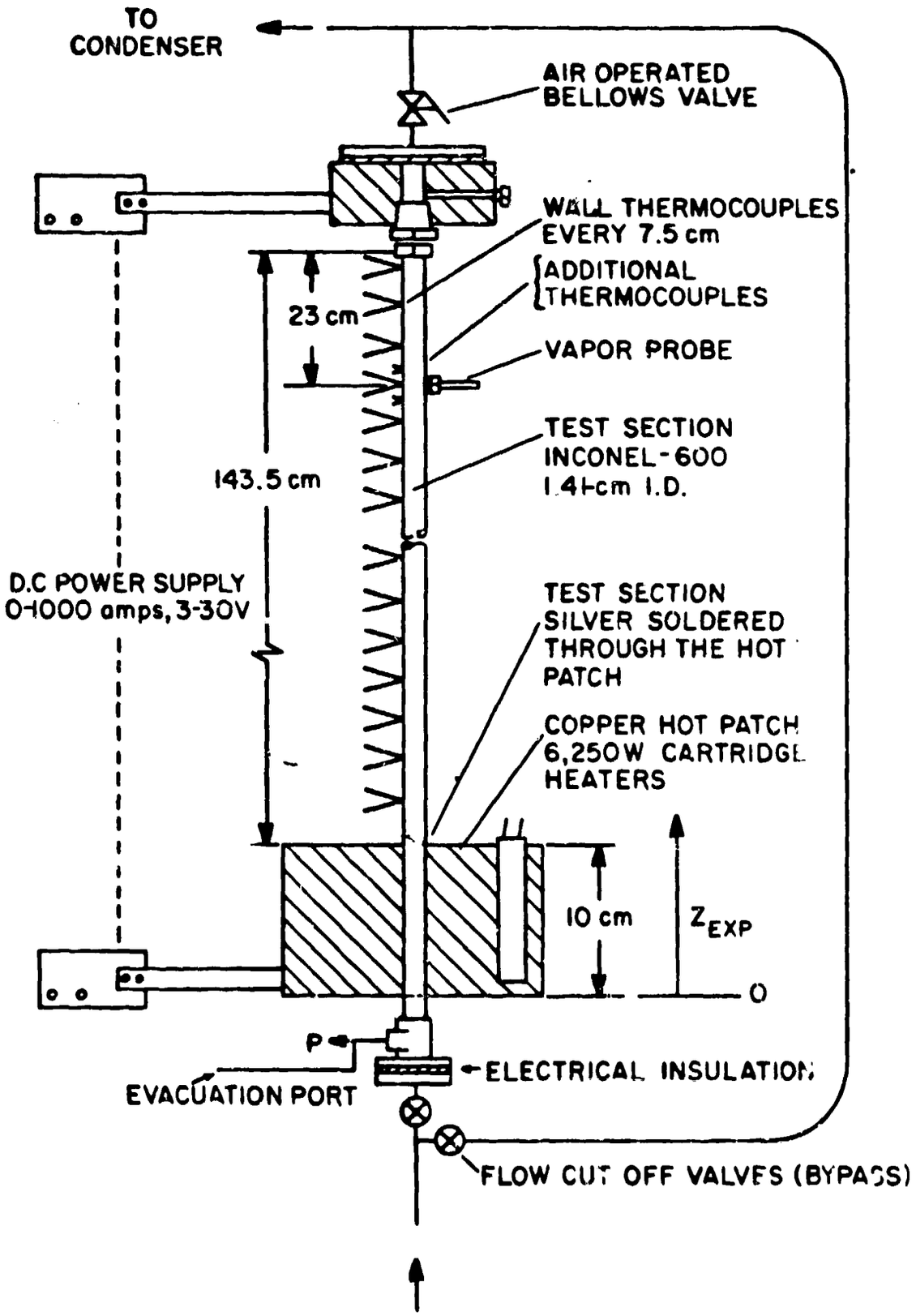

Fig. 1. Lehigh University experimental test facility for post-CHF heat transfer.

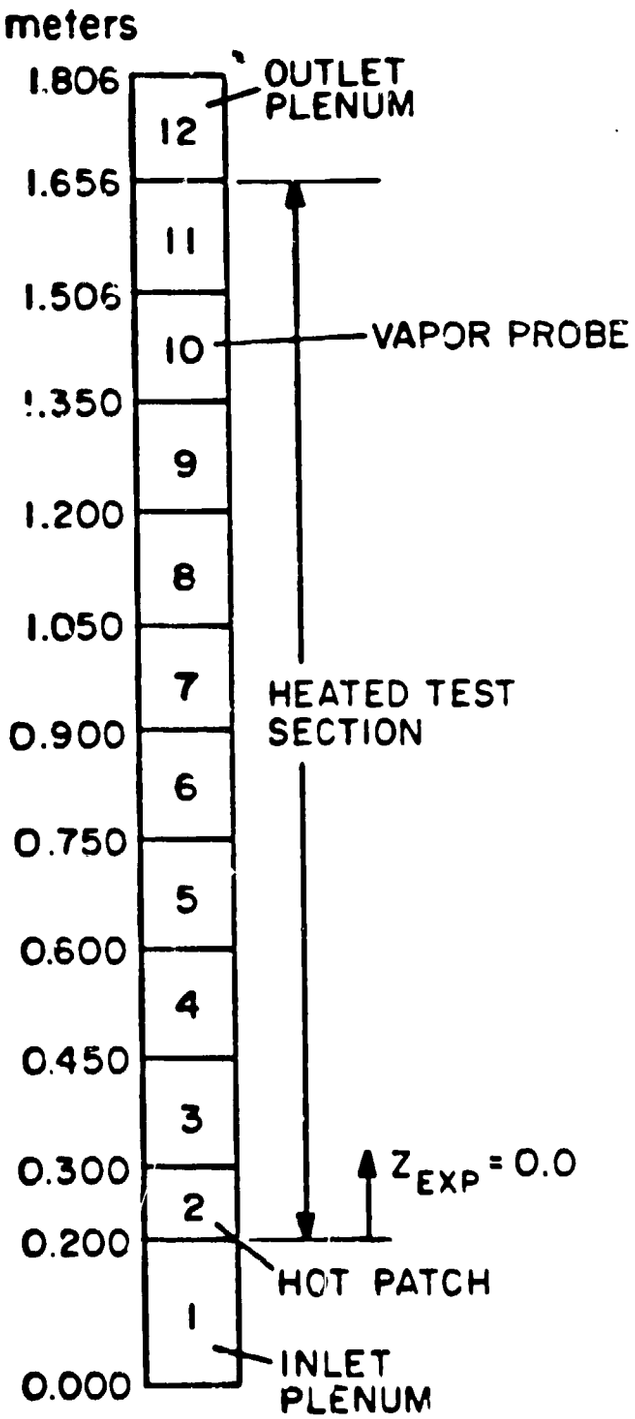

Fig. 2. Input model of the Lehigh University experimental test facility.

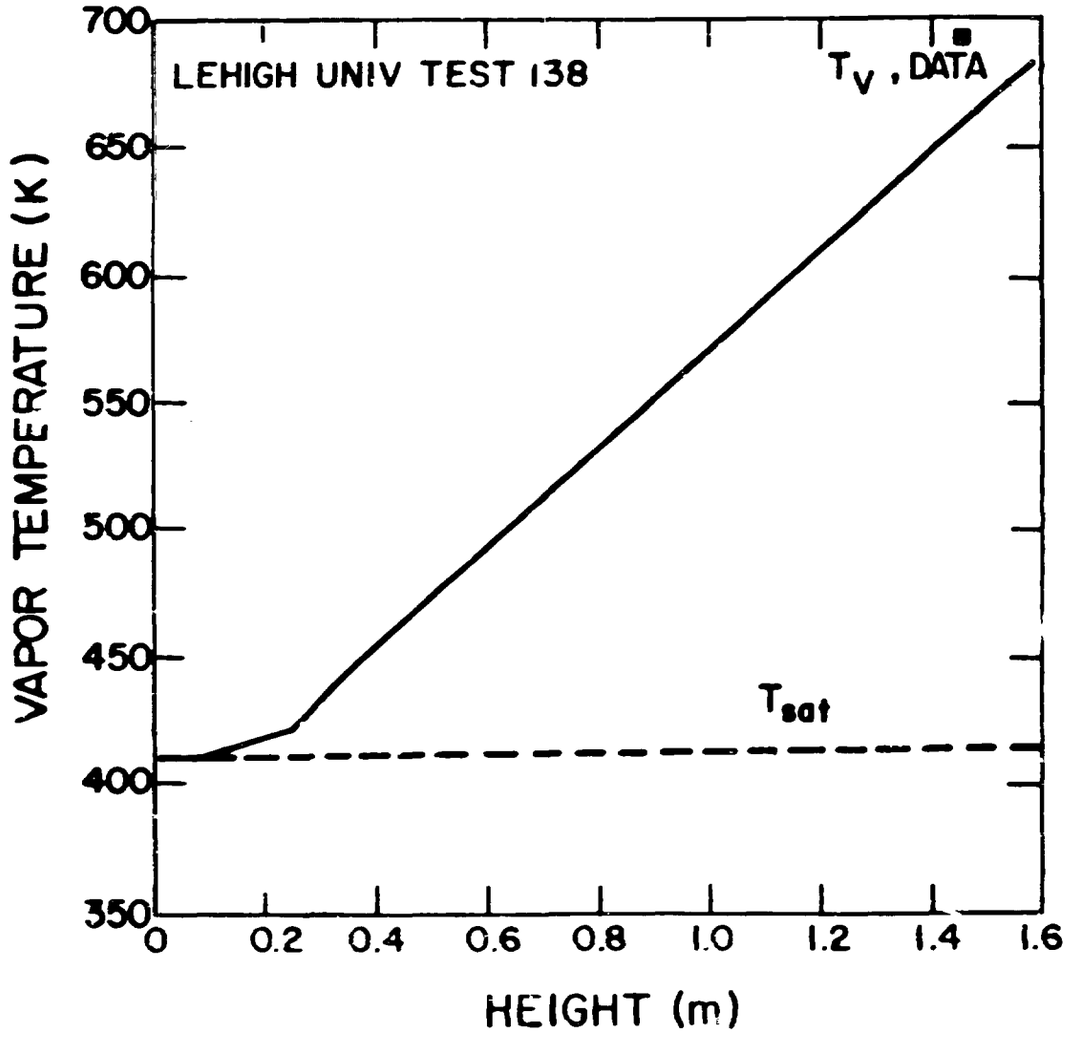

Fig. 3. Comparison between calculated and measured vapor temperature for test 138.

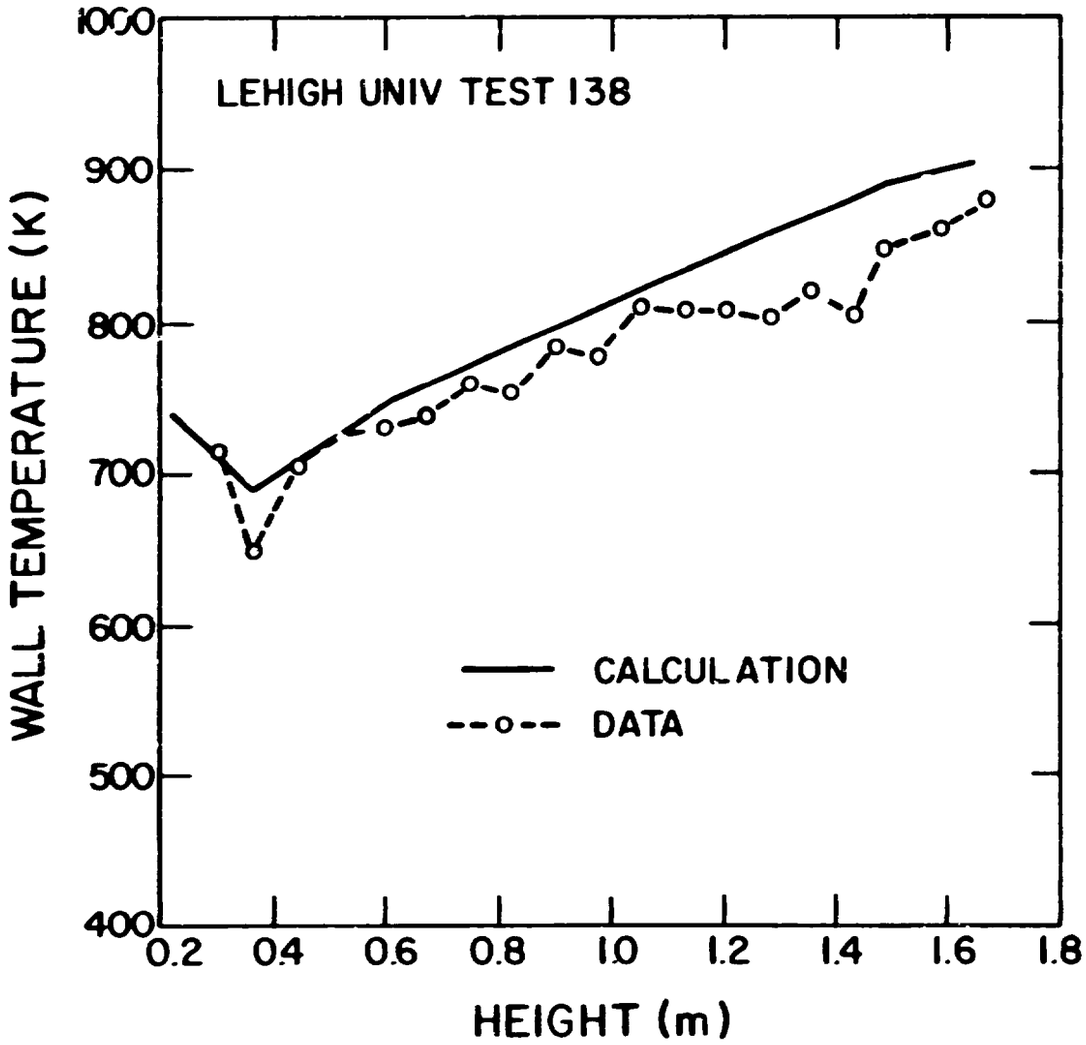

Fig. 4. Comparison between calculated and measured wall temperature for test 138.

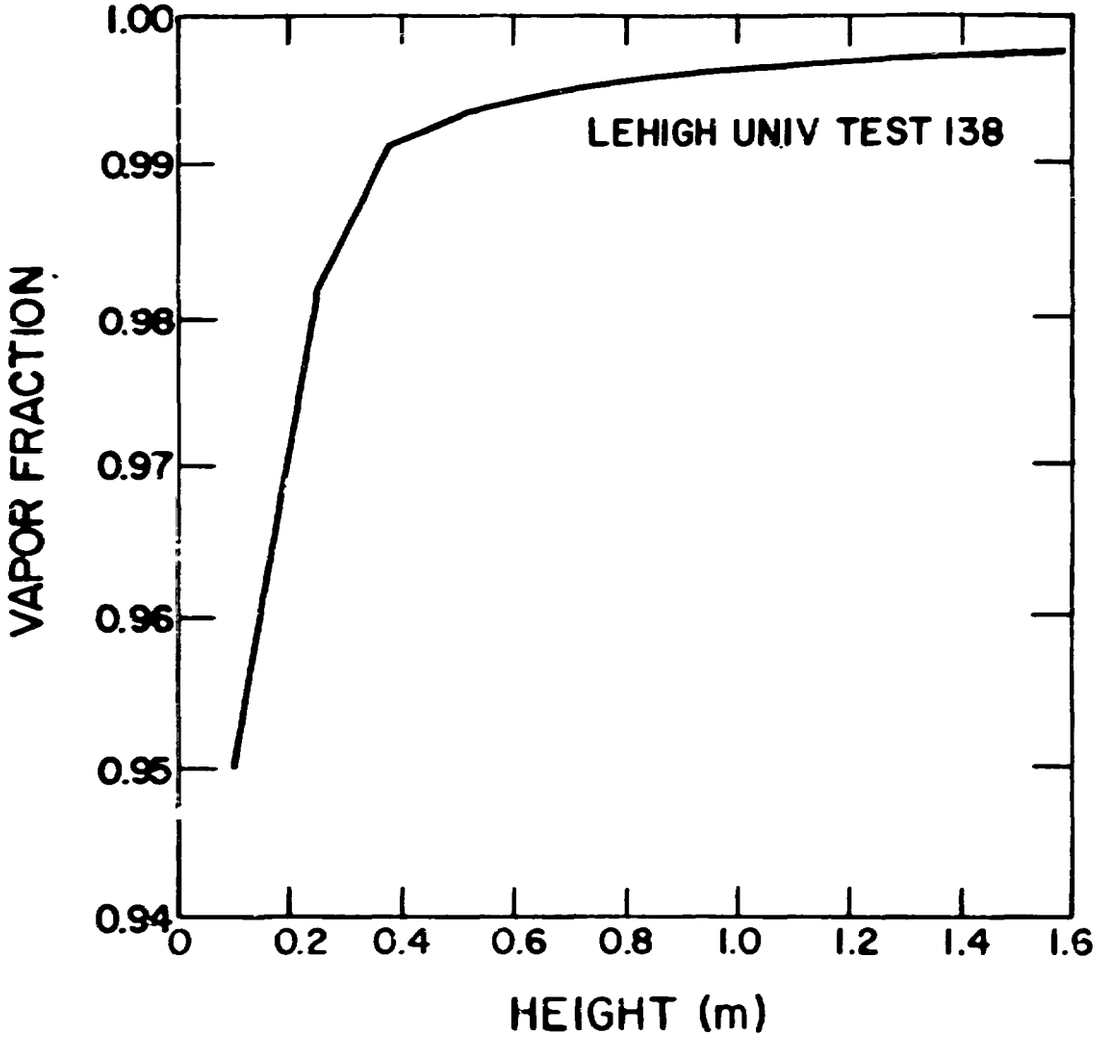

Fig. 5. Calculated vapor volume fraction versus heated length for test 138.

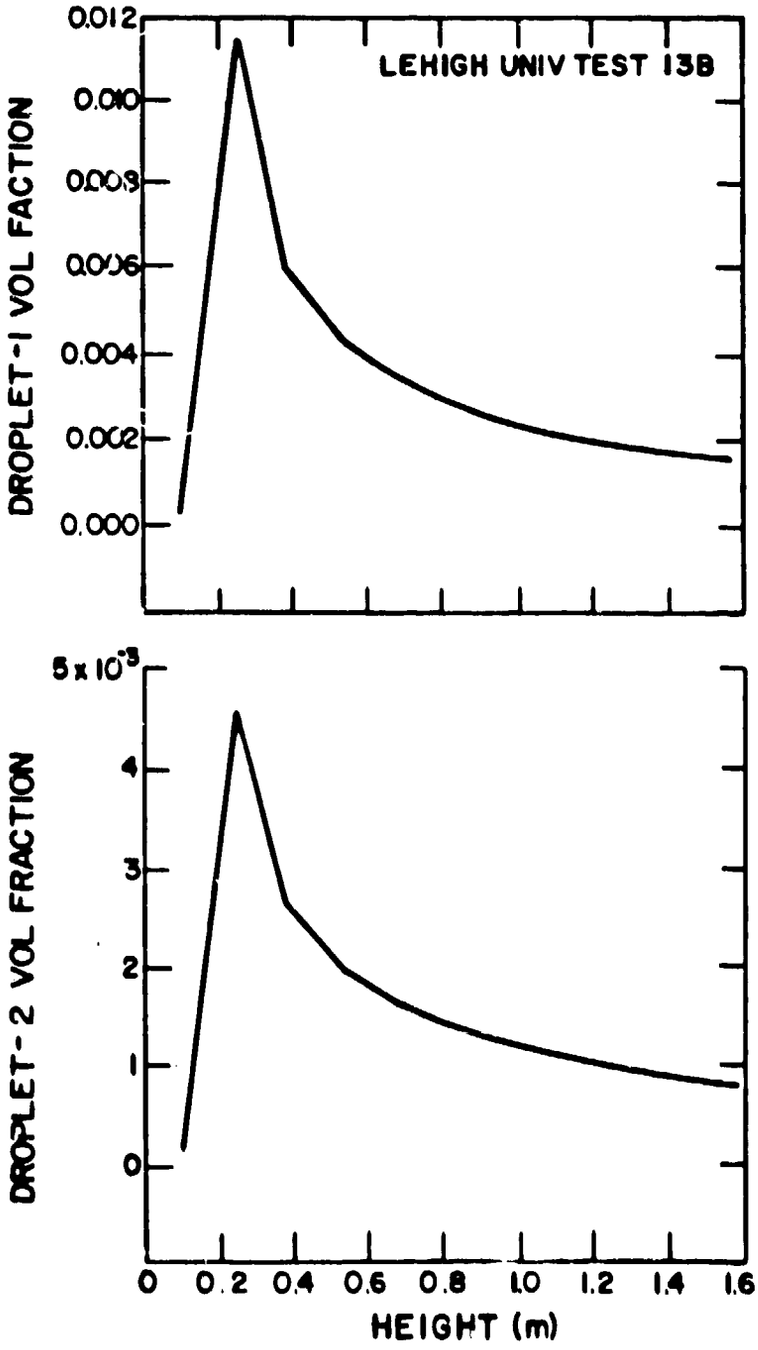

Fig. 6. Calculated droplet fields volume fraction versus heated length for test 138.

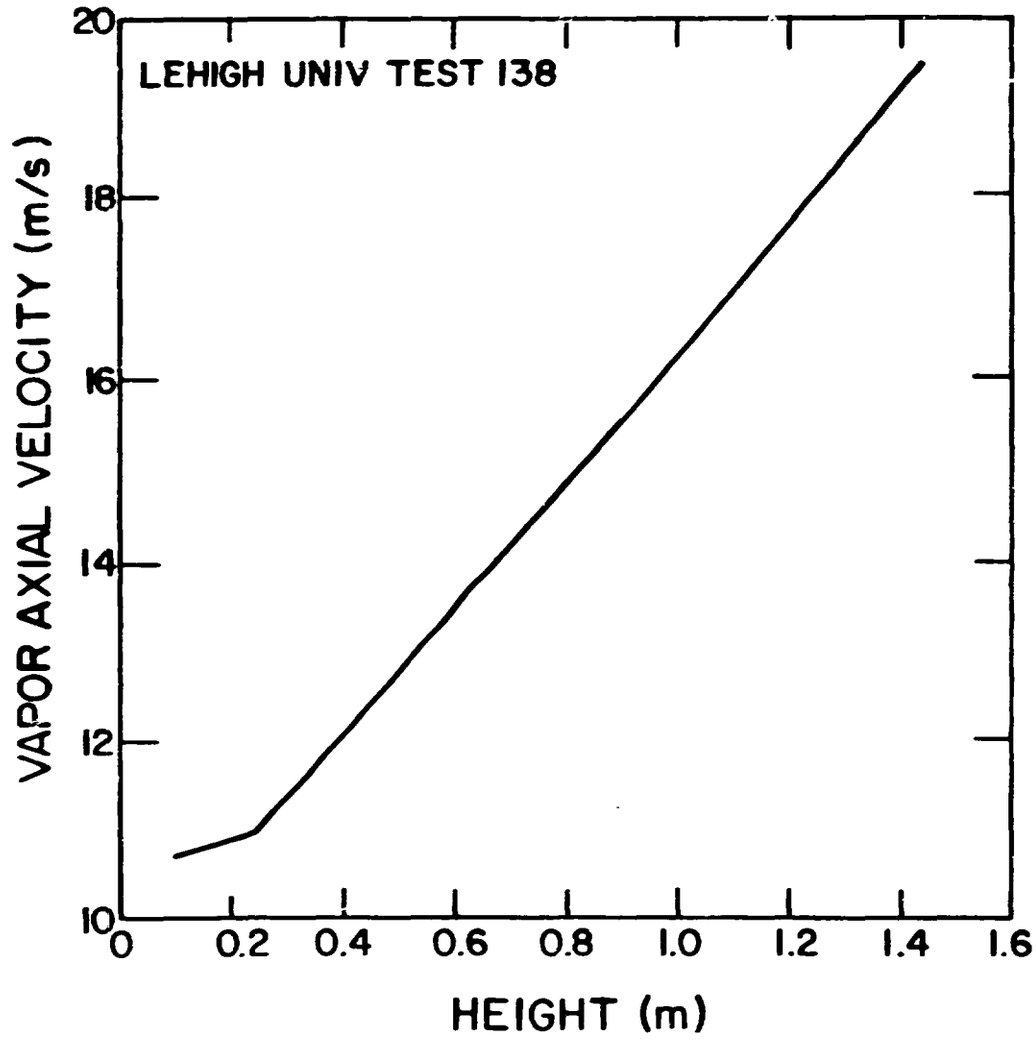

Fig. 7. Calculated vapor velocity versus heated length for test 138.

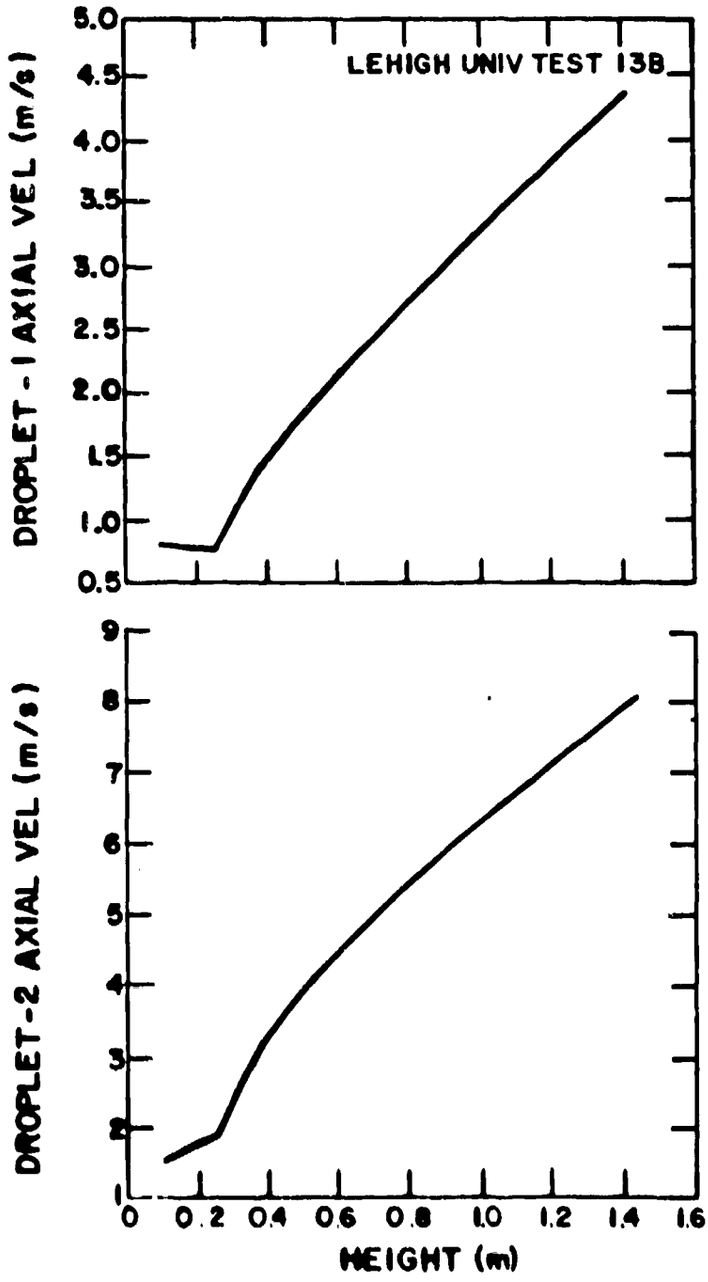

Fig. 8. Calculated droplet velocities versus heated length for test 138.

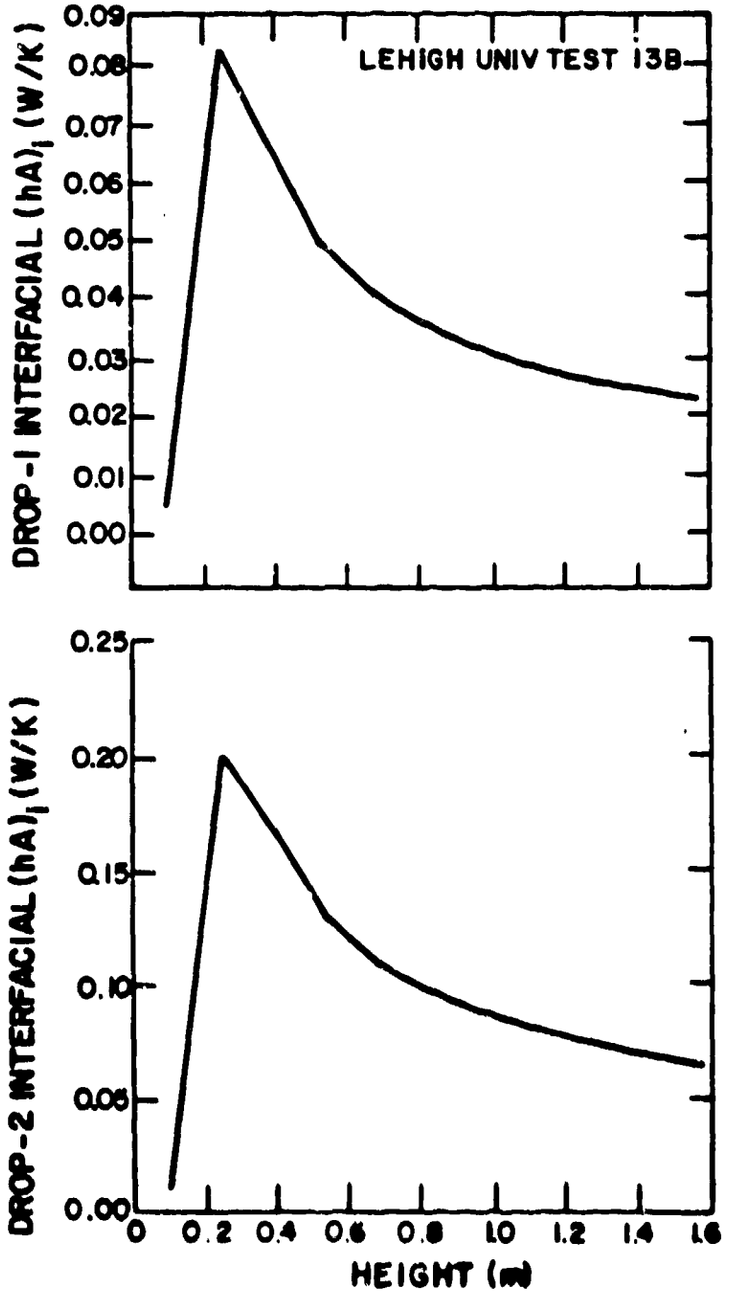

Fig. 9. Calculated interfacial heat transfer coefficient versus heated length for test 138.

Test 138

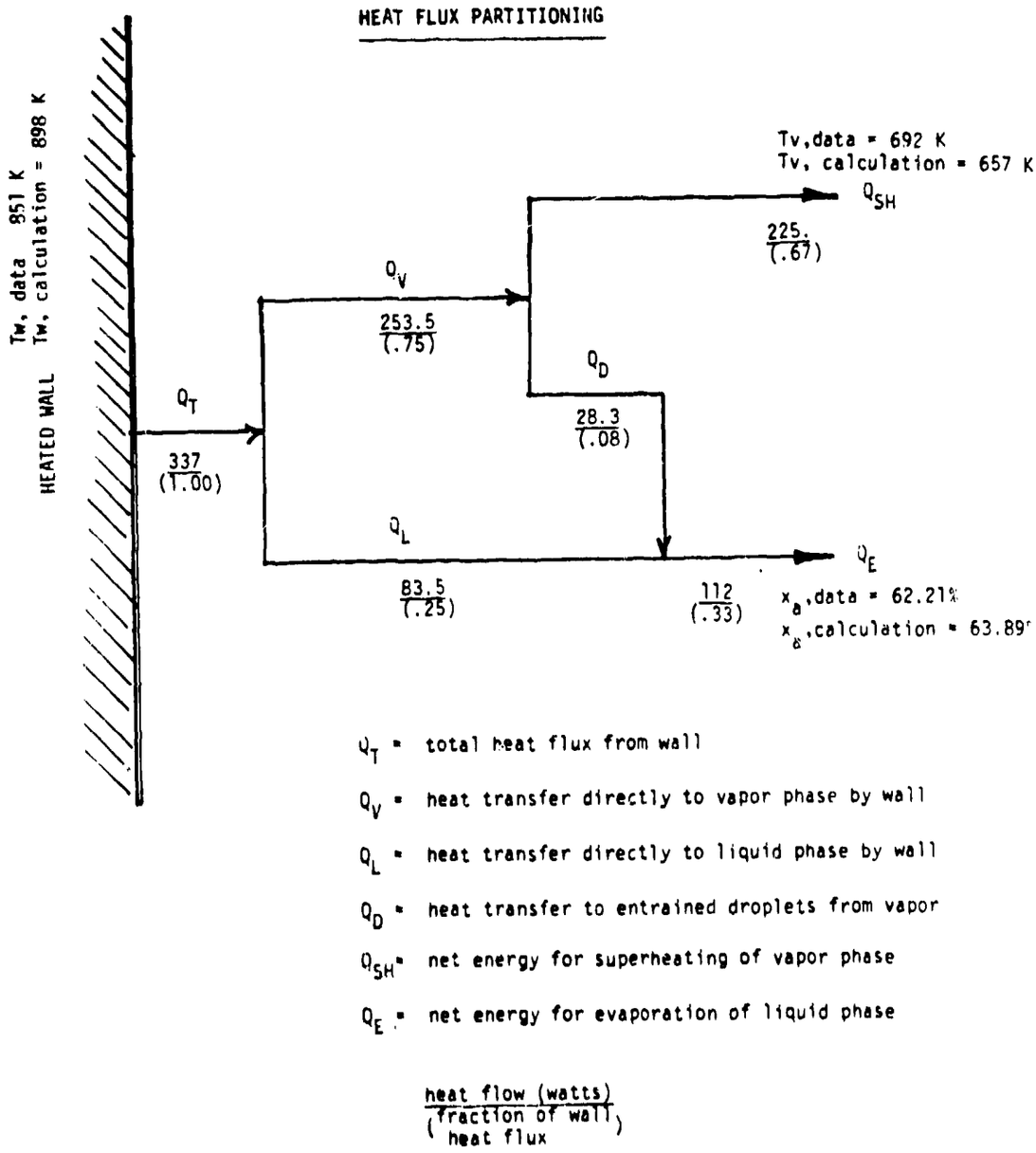

Fig. 10. Calculated heat flow to the vapor and liquid fields at the vapor probe elevation.

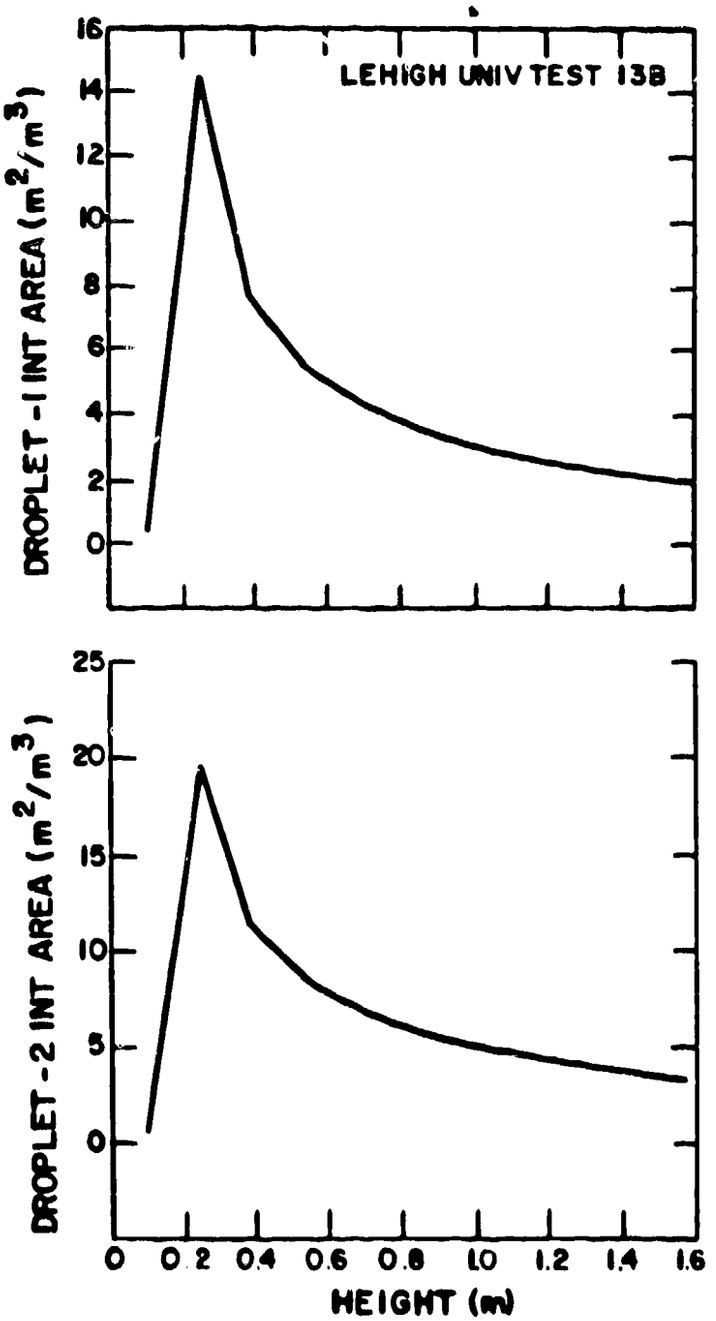

Fig. 11. Calculated droplet interfacial area concentration versus heated length for test 138.

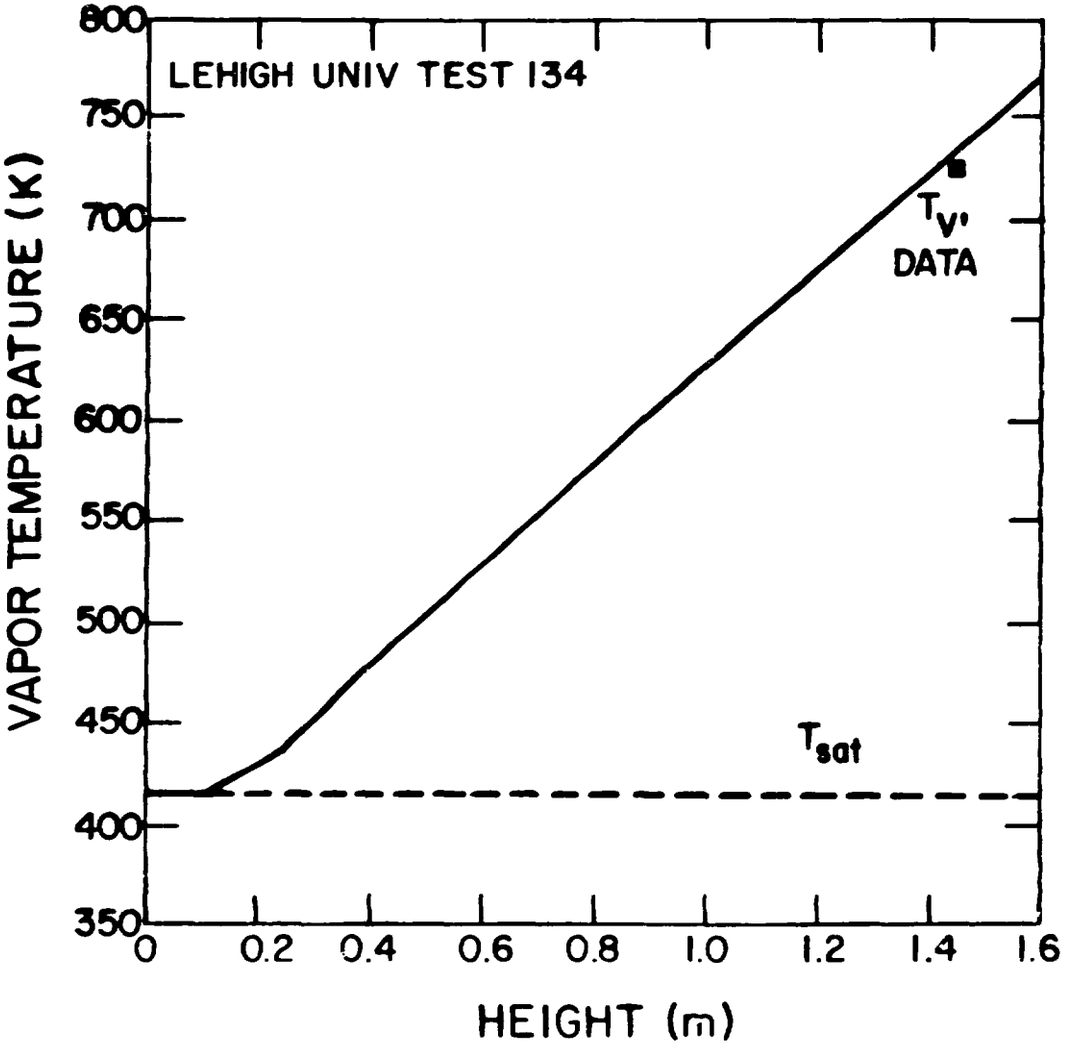

Fig. 12. Comparison between calculated and measured vapor temperature for test 134.

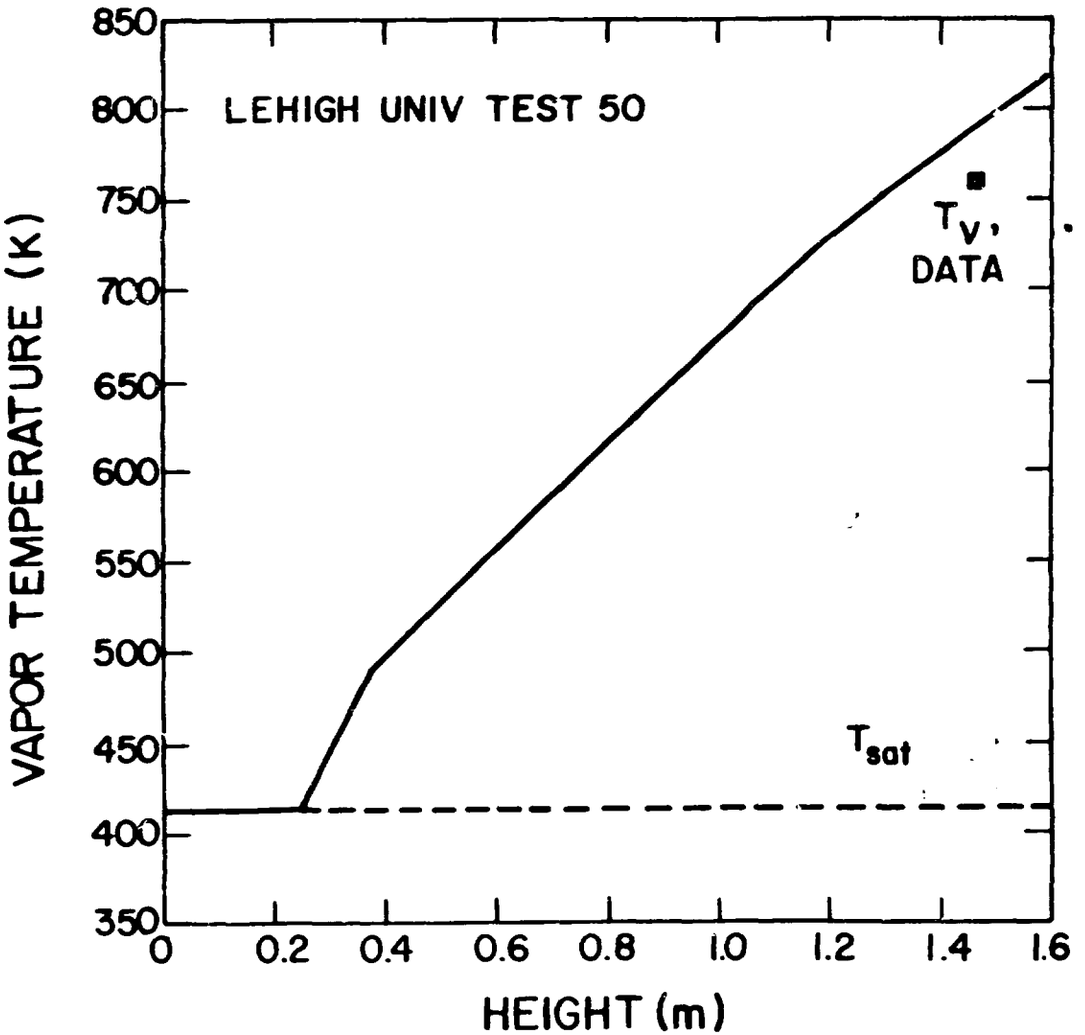

Fig. 13. Comparison between calculated and measured vapor temperature for test 50.